Optomechanical spring enhanced mass sensing

Maksymowych, M. P.; Westwood-Bachman, J. N.; Venkatasubramanian, A.; Hiebert, W. K.

Publisher's version / Version de l'éditeur:
https://doi.org/10.1063/1.5117159
Applied Physics Letters, 115, 10, pp. 101103-1-101103-5, 2019-09-03

Optomechanical Spring Enhanced Mass Sensing

M. P. Maksymowych,[1,2] J. N. Westwood-Bachman,[1,2,a)] A. Venkatasubramanian,[1,3,b)] and W. K. Hiebert[1,2,c)]

[1] *Nanotechnology Research Centre, National Research Council of Canada, 11421 Saskatchewan Drive, T6G 2M9, Edmonton, Canada*

[2] *Department of Physics, University of Alberta, Edmonton, T6G 2E1, Canada*

[3] *Department of Biological Sciences, University of Alberta, Edmonton, T6G 2R3, Canada*

On-chip nano-optomechanical systems (NOMS) have demonstrated zeptogram-level mass sensitivity and are promising candidates for low-cost implementations in areas such as metabolite quantitation and chemical analysis. High responsivity and sensitivity call for substantial optomechanical coupling and cavity finesse, resulting in detuning-dependent stiffness and mechanical damping via optomechanical back-action. Since mass loading (or temperature or force change) can alter both mechanical and cavity properties, mechanical frequency shifts induced by loading can encompass both effects. Precision sensing requires understanding and quantifying the source of the frequency tuning. Here, we show deconvolution of direct loading and optomechanical stiffness change on the mechanical eigenfrequency as a function of detuning for a nano-optomechanical sensor in gaseous sensing experiments. Responses were generally dominated by shifts in optical stiffness and resulted in mass loading signal amplification by as much as a factor of 2.5. This establishes an alternative possible route toward better mass sensitivity in NOMS while confirming the importance of incorporating optical stiffness effects for precision mass sensing.

On-chip nano-electromechanical systems (NEMS) and nano-optomechanical systems (NOMS) [1-3] have been established as ultrasensitive mass detectors [4], viable for future implementations in a multitude of areas ranging through metabolite quantitation [5-6], gas chromatography [5-8], mass spectrometry [9-15], and environmental monitoring [16]. On-chip optomechanics has also become a popular candidate for force sensing [17-21] and thermometry [22]. An approach to NOMS sensitivity improvement by decreasing modal mass is enabled by increasing optomechanical coupling [23]. Larger optomechanical coupling comes with substantial back-action in which mechanical stiffness and damping are altered by the optical cavity forces [2] in a way that depends strongly on cavity detuning. A common NEMS sensing principle is that mass loading leads to a change in mechanical eigenfrequency [24] (or

a) Present address: Applied Nanotools Inc., 11421 Saskatchewan Drive, T6G 2M9, Edmonton, Canada
b) Present address: Department of Biomedical Engineering, University of Michigan, 1101 Beal Avenue, Ann Arbor, Michigan 48109, USA
c) Author to whom correspondence should be addressed. Electronic mail: Wayne.Hiebert@nrc-cnrc.gc.ca

mechanical damping), for instance during analyte binding or loading. This same loading also shifts the optical cavity resonance, causing a change in the optomechanical spring constant and damping that can obscure the direct loading effect. As such, back-action can potentially result in imprecise or inconsistent mass sensing. Optical spring sensing has been employed in niche configurations such as high Q optomechanical crystals [25] and microspheres [26]. These reports focused on cavity shift sensing properties rather than mechanical loading. There has been little focus on the pervasive role that optomechanical rigidity plays in optomechanical sensor precision over the entire cavity detuning space. In this letter, we report precision measurements of the optomechanical spring effect and use it to deconvolve and calibrate mass loading over the full cavity detuning range. We employed a moderately coupled cantilever-racetrack NOMS, and account for a back-scattered (split) nonlinear cavity to characterize the impact of shifting optical stiffness in gas sensing and thermometry experiments. We were able to extract frequency changes of opposite sign caused by direct loading versus changing optical stiffness. Responses were dominated by shifts in optical stiffness, resulting in a response signal amplification factor of up to approximately 2.5. Due to the optical spring, roughly equal analyte load amounts triggered vastly different frequency shifts of +150 Hz, +964 Hz, and -1000 Hz, which can be corrected to effective direct loading shifts of -493 Hz, -454 Hz, and -420 Hz, respectively, using our deconvolution and calibration. This technique will enable more precise mass, force, and temperature sensing in NOMS, while also providing a new route to signal enhancement.

A mechanical resonator coupled to a nearby optical cavity modulates the effective refractive index of the cavity, shifting its resonance frequency ω_{cav} [3, 27-29] with optomechanical coupling strength $G = \partial\omega_{cav}/\partial x$. The resulting variation in optical gradient force F_{opt} exerted by the cavity field on the mechanical element in-phase with mechanical oscillation exerts back-action. A mechanical oscillator with modal mass m_{eff} will experience an optomechanically induced stiffness $k_{opt} = -\partial F_{opt}/\partial x$ and a proportional shift in mechanical eigenfrequency $\delta\Omega_m \equiv \sqrt{k_{opt}/m_{eff}}$ in accordance with:

$$\delta\Omega_m(\Delta) = \frac{4P_{bus}}{\hbar\omega_l}\left\{\frac{{g_{o,1}}^2\gamma_{ex,1}(\Delta-\delta_1)}{[(\Delta-\delta_1)^2+{\gamma_1}^2]^2} + \frac{{g_{o,2}}^2\gamma_{ex,2}(\Delta-\delta_2)}{[(\Delta-\delta_2)^2+{\gamma_2}^2]^2}\right\} \quad (1)$$

for an optical cavity that is split into two closely spaced uncoupled resonances (see supplementary material) [30]. The adjacent blue and red cavities are associated with input coupling decay rates $\gamma_{ex,1}$ and $\gamma_{ex,2}$, detuning offsets δ_1 and δ_2, total cavity amplitude decay rates γ_1 and γ_2, and single-photon coupling strengths $g_{o,1}$ and $g_{o,2}$, respectively, where $\Delta \equiv \omega_l - \omega_{cav}$ is the cavity detuning, ω_l is the input laser frequency and P_{bus} is the input (bus waveguide) power. The coupling strength can be extracted from equation 1 via $G = g_0/x_{ZFP}$, where $x_{ZPF} = (\hbar/2m_{eff}\Omega_m)^{1/2}$ is the zero-point amplitude of the mechanical oscillator. For an optomechanical system at fixed Δ, red detuning ($\Delta < 0$) decreases the optical rigidity of the mechanical oscillator, decreasing its eigenfrequency; while blue detuning ($\Delta > 0$) induces stiffening, increasing the eigenfrequency.

To assess the optomechanical spring's influence on NOMS sensing precision, we designed a moderately coupled, high finesse (~270) cantilever-racetrack NOMS device arranged in an all-pass configuration as seen in figure 1a. The thickness of the silicon-on-insulator (SOI) cantilever and waveguides was 220 nm, lying on a 2 μm buried oxide wafer. The nanomechanical cantilever was 130 nm wide and 3.9 μm long, corresponding to a fundamental flexural mode eigenfrequency of 10.7 MHz and a modal mass of 64.9 fg. The cantilever-racetrack gap spacing was 130 nm for moderate optomechanical coupling [23]. Our photonic cavity was slightly overcoupled, with a 7.12nm free spectral range. The cavity resonance depicted as green in figure 1b was acquired at 298 K using a Santec TSL-510 tunable diode probe laser scanned from 1513.65 - 1513.90 nm with 108 μW in the bus waveguide, and was modelled by a nonlinear split cavity Lorentzian fit [30]. Splitting arises from contra-directional eigenmode interference initiated by coherent backscattering off surface roughness [30, 31]. Changes to cavity refractive index shift the resonance without alterations in cavity properties (see figure S13). Our nanophotonic transduction scheme is detailed in [32]. The total cavity decay rate $\gamma/2\pi$

of 3.08 GHz is much larger than our cantilever frequency 10.7 MHz. Therefore, our device operates in the Doppler regime where equation 1 is valid, dissipative optomechanical backaction is suppressed [33], and dispersive dynamical backaction induced optomechanical damping $\Gamma_{opt} \propto \gamma^{-3}$ is negligible [29] (see supplementary material). Intrinsic thermomechanical (TM) noise was measured as a function of cavity detuning while the device was in vacuum (~10^{-4} Torr). The NOMS fundamental eigenfrequencies were extracted by Lorentzian fitting each TM noise sweep. The eigenfrequency at -13.6 GHz detuning, where the optical stiffness is negligible, was selected as a reference frequency and the shifts relative to it $\delta\Omega_m(\Delta)$ are shown as black in figure 1b. The theoretical fit of the frequency shift data to equation 1 shown in blue yielded optomechanical coupling strengths $G_1/2\pi$ of 0.274 GHz/nm and $G_2/2\pi$ of 0.074 GHz/nm. The optical nonlinearity present on the red side due to sufficiently high optical power results in an artificially high slope and low coupling strength G_2 associated with the fit to equation 1. The presence of 3 – 4 kHz shifts confirms the existence of a substantial optomechanical spring interaction.

The NOMS frequency response to analyte adsorption was assessed in atmospheric pressure (mechanical Q ~ 20) at 298 K. Our photonic chip was mounted via epoxy onto a shear-mode piezoelectric crystal for mechanical actuation to achieve high signal to noise ratio, sensitivity and transduction, while maintaining linear operation (see supplementary material). The driven response was monitored via nanomechanical phase-locked loop on a Zurich HF2LI Lock-in Amplifier using LabOne software while applying a 320 mV piezo-drive voltage, which was amplified by 34 dB using a GW INSTEK GPR-30600 amplifier. Gas chromatography (GC) equipment was employed to deliver separated analyte loaded carrier gas into the device chamber as described in [5]. At 16 probe detuning setpoints, a 1 µL injection of a volatile organic compound (VOC) mixture containing 1 mL of hexane solvent, 3.42 mg of benzene, 3.57 mg of toluene, 3.55 mg of xylene, and 3.44 mg of mesitylene was sent through the GC and delivered in vapor form to the device at a fixed continuous flow rate. Separated eluant peaks indicate VOC concentration changes on a timescale of seconds. The probe laser wavelength

was constant during a given GC test. The NOMS cantilever and photonic racetrack both act as sensors, which sample the local concentration of sub-zeptogram mass analytes delivered by the GC stream. The photonic element detects analyte clouds present in the evanescent volume and adsorbed on the photonic sensor surface via a resonance shift. The cantilever senses mass accumulated on its surface [15] convolved with change in optomechanical stiffness caused by the cavity resonance shift. In all NOMS GC experiments the concentrations of analytes sent in were constant, implying that eluent peaks arriving at the NOMS detector should always be associated with about the same amount of mass. Thus, any significant difference in NOMS response between probe points should be attributed to an effect other than analyte mass loading on the cantilever.

Figure 2 displays the NOMS eigenfrequency f_m (MHz) at probe laser detunings of 7.08 GHz (light blue), 3.52 GHz (red), -2.22 GHz (black), -3.95 GHz (dark blue) and -4.94 GHz (pink) on a common frequency scale over time (s) as analyte vapor was delivered to the nanosensor. The corresponding probe setpoints are marked on the cavity transmission (mV) spectrum in detuning space (figure 2 inset). The positive and negative frequency responses between detunings cannot be explained by mass loading alone, which is expected to cause a drop in eigenfrequency at all probe points. Responses are instead dominated by shifts in optical stiffness, which are caused by the presence of analytes within the evanescent field of the cavity. VOC analyte induces a local refractive index increase by ~0.5 (compared to ambient air), which lengthens the optical path and shifts the cavity resonance relative to the constant probe. Analyte refractive indices are included in the supplementary material. During gas sensing, helium carrier gas from the GC thermal oven constantly flows over the NOMS, indicating that the response is due to a refractive index shift caused by gaseous analytes, and not temperature shifts. The change in optical stiffness depends on the initial and final probe detunings leading to spring stiffening or softening (equation 1). Optical stiffness change and the direct mass loading are separate effects that combine to give the total frequency shift during eluent peak loading. The signal peaks vary substantially in both

magnitude and sign. Peak ratios are also affected: in the case of -2.22 GHz, the xylene peak signal is about 10x that of toluene, whereas it is about 1x at 3.52 GHz detuning. There is a clear need for deconvolution of mass signal from the spring change signal in order to perform reliable mass measurements.

The NOMS frequency response component due to the shift in optical spring $\delta f_{m,\ opt}$ was determined by using a reference spring detuning curve interpolation from the discrete TM noise eigenfrequency datapoints $\delta\Omega_m(\Delta)$ of figure 1b. The eigenfrequencies at the initial laser detuning Δ_i and the inferred final detuning $\Delta_f{}'$ were subtracted to extract the optical spring component:

$$\delta f_{m,\ opt} = \delta f_m(\Delta_f{}') - \delta f_m(\Delta_i) \tag{2}$$

where $\delta f_m(\Delta) = \delta\Omega_m(\Delta)/2\pi$. The detunings Δ_i and Δ_f correspond to the initial V_i and final V_f ($\delta V \equiv V_f - V_i$) measured cavity throughputs directly before and after adsorption that were obtained by monitoring ring transmission in real-time. The optical cavity resonance datapoints were interpolated to determine Δ_i and Δ_f ($\delta\Delta \equiv \Delta_f - \Delta_i$). Since a constant amount of toluene was delivered to the nanosensor, the average shift in laser detuning $\delta\Delta_{ave}$ (0.541 GHz) was utilized to compute the inferred final detuning $\Delta_f{}'$ according to: $\Delta_f{}' = \Delta_i + \delta\Delta_{ave}$. The total observed eigenfrequency shift δf_m together with $\delta f_{m,\ opt}$ give an approximate shift due to mass loading $\delta f_{m,\ mass}$ via the equation: $\delta f_{m,\ mass} \approx \delta f_m - \delta f_{m,\ opt}$. NOMS mass sensitivity was approximated using the equation: $\delta m = -2m_{eff}\delta f_m/f_m$.

The NOMS mechanical eigenfrequency f_m (MHz) near toluene adsorption is displayed in figure 3 over time (s). At 3.52 GHz (red), -2.22 GHz (black), and -3.95 GHz (blue) cavity detunings, the adsorption of roughly equal amounts of toluene triggered eigenfrequency shifts of 150 Hz, 964 Hz, and -1000 Hz, respectively. Assuming this was all direct mass loading, these shifts would correspond to masses of -1.82 ag, -11.7 ag, and 12.2 ag sensed. A negative amount of mass detected during loading clearly indicates that another effect is in play. After correcting for the optical stiffness, the frequency

shifts due to toluene loading are approximately -493 Hz, -454 Hz, and -420 Hz corresponding to masses of 5.99 ag, 5.52 ag, and 5.10 ag, respectively (represented as thin traces in figure 3). Consistency and precision in NOMS mass sensitivity is achieved only after accounting for the optical spring, which induces dramatic signal amplification or cancellation. Depending on the detuning, the optomechanical spring change provides signal enhancement by as much as a factor of 2.5 times over the bare mass loading signal.

Temperature responsivity [4] of the NOMS was calibrated using a 500 mW CL-2000 continuous crystal laser (1064 nm) to validate consistency in our calibration of $\delta\Delta$. A fixed highly localized heat flux of roughly 0.62 μW/μm^2 was steadily delivered to the device surface using a CaF_2 collimator lens and two attenuating filters with optical densities of 0.5 and 1.0. The thermo-optic effect causes a decrease in cavity resonant frequency ω_{cav}, shifting the cavity relative to the constant probe in a similar fashion to analyte adsorption. The cavity responses δV (mV) to toluene adsorption (blue) and laser heating (orange) as a function of detuning are depicted on separate voltage scales with the point derivative of the cavity transmission spectrum $\partial T/\partial\Delta$ (black) in figure 4a. Cavity throughput responses vary in accordance with $\partial T/\partial\Delta$ as expected. Toluene (blue) and heat (orange) induced detuning shifts $\delta\Delta$ (GHz) are plotted across cavity detuning space in figure 4b and are situated within constant horizontal bands, giving average detuning shifts $\delta\Delta_{ave}$ of 0.541 GHz and 0.217 GHz, respectively. The uniformity in $\delta\Delta$ across the cavity validates our detuning interpolation scheme and confirms consistency in the amount of toluene/heat being delivered to the sensor.

NOMS responses to toluene adsorption (blue data points) across the full detuning landscape are depicted in figure 4c. The expected optomechanical spring induced frequency shift, $\delta f_{m,\ opt}$, from the toluene loading on the optical racetrack is overlaid (thick black line). The latter curve was constructed using equation 2 along with the TM noise dependence on detuning. This same curve is offset as a shadow (thick red line) by the nominal direct mass loading amount of -456 Hz. The resulting thick red

curve, $\delta f_{m,\ opt}$ – 456 Hz, which accounts for both the optomechanical spring and mass loading, should track well to the measured total frequency shifts induced by the toluene, δf_m, which it does. The NOMS responses are precisely situated along the shadowing curve separated from $\delta f_{m,\ opt}(\Delta_i)$ by the average deconvolved shift due to mass loading $\overline{\delta f}_{m,mass} \approx$ - 456 Hz, most of them falling within error bounds. Residual variation in responses after deconvolution can be at least partially attributed to the perturbation in cavity resonance lineshape and overall throughput (and therefore the TM noise data) with each confocal system alignment [32]. At large absolute values of detuning, inordinately large negative adsorption responses were observed, accompanied by excess drift in baseline eigenfrequency over time and substantial frequency fluctuation noise, as encapsulated by the large error bars in figure 4c. These large responses are far from probe points used for sensing applications and their source, possibly due to second order optomechanical coupling [34], is a current topic of investigation. For gas sensing applications of NOMS, typically utilized probe points are where cavity transmission slope is high, enabling optimal photonic transduction [23]. These probe points are simultaneously the most susceptible to shifts in optical rigidity during sensing, especially in a highly coupled sensor.

Thorough characterization of the optomechanical spring together with our deconvolution methodology offers a new route to high precision mass and temperature sensing with predictable signal enhancement, provided that $\delta\Delta$ is small. Laser setpoints of high optical spring slope $\partial\Omega_m/\partial\Delta$ (figure 1b), where optomechanical stiffness is highly sensitive to cavity resonance shifts, allow for enhanced mass responsivity. For instance, the highest slope point of the optical spring detuning curve (figure 1b) is at -2.22 GHz with a value $\partial\Omega_m/\partial\Delta$ of +2.12 kHz/GHz. The deconvolved toluene loading response of -454 Hz corresponds to a mass of 5.52 ag which, by typical definition, implies a mass responsivity of -82.3 Hz/ag. Using the optical spring tuning allows us to define an effective optomechanically induced responsivity due to the optical spring effect:

$$\left(\frac{\delta f_m}{\delta m}\right)_{opt} \equiv \left(\frac{\partial\Omega_m}{\partial\Delta}\right) \times \left(\frac{\delta\Delta/2\pi}{\delta m}\right) \propto P_{bus} G^2 \gamma^{-3} \tag{3}$$

The toluene mass loading on the ring causes an average detuning shift of $\delta\Delta/2\pi$ ~ 0.541 GHz. This results in an effective responsivity of +208 Hz/ag at -2.22 GHz detuning, whose magnitude is a factor 2.5 higher than the direct loading responsivity. This responsivity can be dramatically enhanced by increasing P_{bus}, G, and decreasing γ, ultimately making the direct mass loading increasingly trivial. For example, removing optical nonlinearity concerns by moving to a similar diamond optomechanical system [35], a factor of 10 improvement in each variable would increase the responsivity by a million-fold to 200 Hz/yg.

Nano-optomechanical devices exhibit a high degree of transduction, sensitivity, and optomechanically induced stiffness, making them optimal for interaction-based biomedical and chemical sensing applications. By accounting for the optical stiffness in optomechanical gas sensing, the response signal is amplified by a factor of up to 2.5 without alterations in sensor design, while precision is restored to sensed mass. Specifically, at 3.52 GHz, -2.22 GHz, and -3.95 GHz cavity detunings, the adsorption of roughly equal amounts of toluene induced total eigenfrequency shifts of 150 Hz, 964 Hz, and -1000 Hz respectively, corresponding to masses of -1.82 ag, -11.7 ag, and 12.2 ag sensed. After correcting for the optical stiffness, the direct loading frequency shifts are approximately -493 Hz, -454 Hz, and -420 Hz corresponding to masses of 5.99 ag, 5.52 ag, and 5.10 ag, respectively. Consistency and precision in NOMS mass sensitivity and frequency response is achieved only after incorporating optical stiffness variation. The inclusion of optical rigidity in thermometry and gas sensing readout makes a reliable optomechanical sensor substantially easier to achieve. Furthermore, higher optical drive power and optomechanical coupling is expected to provide increasingly enhanced sensor responsivity.

AUTHOR CONTRIBUTIONS

M.P.M. performed the experiments, created the deconvolution model, analysed and interpreted the data, and composed the manuscript, figures and supplementary material all in consultation with W.K.H., the project supervisor. J.N.W.-B. designed the device, formulated the split cavity models, and together with much help from A.V. aided M.P.M. with the experimental design and execution.

ACKNOWLEDGEMENTS

This work was supported by the National Research Council's Nanotechnology Research Centre (NANO) and its fabrication, microscopy, and characterization facilities; by the Natural Sciences and Engineering Research Council, Canada (Grant Nos. RGPIN-2019-06400, 356093-2013, and USRA program (M.P.M.)); by the Vanier Canada Graduate Scholarship program (J.N.W.-B.) and by Alberta Innovates (scholarship and collaborative research innovation grant). Device fabrication was facilitated through CMC Microsystems (silicon photonics services and CAD tools) with post-processing at the University of Alberta nanoFAB.

SUPPLEMENTARY MATERIAL

See the supplementary material for a description of the device fabrication, its characterization, photonics and optomechanics theory with equations, relevant optomechanical interactions, fitting procedures and parameters, a detailed explanation of our deconvolution methodology, and a comprehensive account of experimental data acquisition and procedures.

REFERENCES

[1] M. Li, W.H.P. Pernice, C. Xiong, T. Baehr-Jones, M. Hochberg, and H.X. Tang, Nature 456, 480 (2008).

[2] M. Eichenfield, R. Camacho, J. Chan, K.J. Vahala, and O. Painter, Nature 459, 550 (2009).

[3] V.T.K. Sauer, Z. Diao, M.R. Freeman, and W.K. Hiebert, Applied Physics Letters 100, 261102 (2012).

[4] S.K. Roy, V.T.K. Sauer, J.N. Westwood-Bachman, A. Venkatasubramanian, and W.K. Hiebert, Science 360, (2018). [5] A. Venkatasubramanian, V.T.K. Sauer, S.K. Roy, M. Xia, D.S. Wishart, and W.K. Hiebert, Nano Letters 16, 6975 (2016).

[5] A. Venkatasubramanian, V.T.K. Sauer, S.K. Roy, M. Xia, D.S. Wishart, and W.K. Hiebert, Nano Letters 16, 6975 (2016).

[6] A. Venkatasubramanian, V.T.K. Sauer, J.N. Westwood-Bachman, K. Cui, M. Xia, D.S. Wishart, and W.K. Hiebert, ACS Sensors 4, 1197 (2019).

[7] I. Bargatin, E.B. Myers, J.S. Aldridge, C. Marcoux, P. Brianceau, L. Duraffourg, E. Colinet, S. Hentz, P. Andreucci, and M.L. Roukes, Nano Letters 12, 1269 (2012).

[8] M. Li, E.B. Myers, H.X. Tang, S.J. Aldridge, H.C. Mccaig, J.J. Whiting, R.J. Simonson, N.S. Lewis, and M.L. Roukes, Nano Letters 10, 3899 (2010).

[9] S. Dominguez-Medina, S. Fostner, M. Defoort, M. Sansa, A.-K. Stark, M.A. Halim, E. Vernhes, M. Gely, G. Jourdan, T. Alava, P. Boulanger, C. Masselon, and S. Hentz, Science 362, 918 (2018).

[10] E. Sage, M. Sansa, S. Fostner, M. Defoort, M. Gély, A.K. Naik, R. Morel, L. Duraffourg, M.L. Roukes, T. Alava, G. Jourdan, E. Colinet, C. Masselon, A. Brenac, and S. Hentz, Nature Communications 9, (2018).

[11] O. Malvar, J.J. Ruz, P.M. Kosaka, C.M. Domínguez, E. Gil-Santos, M. Calleja, and J. Tamayo, Nature Communications 7, (2016).

[12] M.S. Hanay, S.I. Kelber, C.D. Oconnell, P. Mulvaney, J.E. Sader, and M.L. Roukes, Nature Nanotechnology 10, 339 (2015).

[13] E. Sage, A. Brenac, T. Alava, R. Morel, C. Dupré, M.S. Hanay, M.L. Roukes, L. Duraffourg, C. Masselon, and S. Hentz, Nature Communications 6, (2015).

[14] M.S. Hanay, S. Kelber, A.K. Naik, D. Chi, S. Hentz, E.C. Bullard, E. Colinet, L. Duraffourg, and M.L. Roukes, Nature Nanotechnology 7, 602 (2012).

[15] A.K. Naik, M.S. Hanay, W.K. Hiebert, X.L. Feng, and M. L. Roukes, Nature Nanotechnology 4, 445 (2009).

[16] E. Ollier, R. Barattin, C. Ladner, M. Petitjean, A. Bellemin-Comte, V. Gouttenoire, K. Benedetto, A. Salette, N. David, V. Jousseaume, P. Puget, L. Duraffourg, and E. Colinet, 2015 Transducers - 2015 18th International Conference on Solid-State Sensors, Actuators and Microsystems (TRANSDUCERS) (2015).

[17] P.E. Allain, L. Schwab, C. Misner, M. Gely, E. Mairiaux, M. Hermouet, B. Walter, G. Leo, S. Hentz, M. Faucher, G. Jourdan, B. Legrand, I. Favero, arXiv:1810.06209 [physics.ins-det] (2018).

[18] P.H. Kim, B.D. Hauer, C. Doolin, F. Souris, and J.P. Davis, Nature Communications 7, (2016).

[19] J. Melcher, J. Stirling, F.G. Cervantes, J.R. Pratt, and G.A. Shaw, Applied Physics Letters 105, 233109 (2014).

[20] E. Gavartin, P. Verlot, and T.J. Kippenberg, Nature Nanotechnology 7, 509 (2012).

[21] K. Srinivasan, H. Miao, M.T. Rakher, Davanço Marcelo, and V. Aksyuk, Nano Letters 11, 791 (2011).

[22] T.P. Purdy, K.E. Grutter, K. Srinivasan, and J.M. Taylor, Science 356, 1265 (2017).

[23] V.T.K. Sauer, Z. Diao, M.R. Freeman, and W.K. Hiebert, Nanotechnology 25, 055202 (2014).

[24] K.L. Ekinci, Y.T. Yang, and M.L. Roukes, Journal of Applied Physics 95, 2682 (2004).

[25] F. Pan, K. Cui, G. Bai, X. Feng, F. Liu, W. Zhang, and Y. Huang, ACS Photonics 5, 4164 (2018).

[26] W. Yu, W.C. Jiang, Q. Lin, and T. Lu, Nature Communications 7, (2016).

[27] B.S. Sheard, M.B. Gray, C.M. Mow-Lowry, D.E. Mcclelland, and S.E. Whitcomb, Physical Review A 69, (2004).

[28] F. Tian, G. Zhou, Y. Du, F.S. Chau, and J. Deng, Applied Physics Letters 105, 061115 (2014).

[29] M. Aspelmeyer, T.J. Kippenberg, and F. Marquardt, Reviews of Modern Physics 86, 1391 (2014).

[30] J. N. Westwood-Bachman, Ph.D. thesis, University of Alberta, Edmonton, (2018).

[31] B.E. Little, J.-P. Laine, and S.T. Chu, Optics Letters 22, 4 (1997).

[32] Z. Diao, J.E. Losby, V.T.K. Sauer, J.N. Westwood, M.R. Freeman, and W.K. Hiebert, Applied Physics Express 6, 065202 (2013).

[33] A.K. Tagantsev, I.V. Sokolov, and E.S. Polzik, Physical Review A 97, (2018).

[34] C. Doolin, B.D. Hauer, P.H. Kim, A.J.R. Macdonald, H. Ramp, and J.P. Davis, Physical Review A 89, (2014).

[35] M. Mitchell, B. Khanaliloo, D.P. Lake, T. Masuda, J.P. Hadden, and P.E. Barclay, Optica 3, 963 (2016).

Figure Captions

FIG. 1. (a) Scanning electron microscope (SEM) image of our 3.9 μm long NOMS cantilever embedded near a 10 μm racetrack optical resonator for photonic transduction. (b) The cavity transmission (mV) of the racetrack resonator is plotted in green and exhibits an intensity-dependent optical nonlinearity. The NOMS eigenfrequencies across the cavity relative to a reference detuning of -13.6 GHz are depicted in black. The fit to equation 1 is shown in blue.

FIG. 2. Gas chromatography equipment delivered a consistent 1 μL injection of a 1 mL hexane solvent solution containing a mixture of benzene, toluene, xylene, and mesitylene to the NOMS sensor situated in controlled atmospheric temperature (298 K) and pressure. The NOMS eigenfrequencies during toluene and xylene adsorption f_m (Hz) at various detuned probe points $\Delta/2\pi$ (GHz) are depicted on a common frequency scale and time domain. The baseline eigenfrequencies have been vertically offset for clarity. Inset: The corresponding probe laser setpoints are marked on a DC optical transmission spectrum in detuning space.

FIG. 3. The NOMS mechanical eigenfrequency (MHz) is displayed over time (s) near toluene adsorption. The baseline eigenfrequencies have been vertically offset for clarity as indicated. At 3.52 GHz (red), -2.22 GHz (black), and -3.95 GHz (blue) cavity detunings; toluene adsorption with equal concentrations triggers eigenfrequency shifts of 150 Hz, 964 Hz, and -1000 Hz, respectively, with corresponding masses of -1.82 ag, -11.7 ag, and 12.2 ag sensed. After correcting for optical stiffness, the frequency shifts are approximately -493 Hz, -454 Hz, and -420 Hz (represented as thin traces) corresponding to masses of 5.99 ag, 5.52 ag, and 5.10 ag, respectively.

FIG. 4. (a) The cavity throughput responses δV (mV) to toluene adsorption (blue) and laser heating (orange) across the cavity transmission are plotted using separate voltage scales with the point derivative of the transmission spectrum $\partial T/\partial \Delta$ (mV/GHz) in black. (b) The toluene (blue) and heat (orange) induced detuning shifts $\delta\Delta$ (GHz) are plotted across detuning space, forming constant horizontal bands. (c) The total NOMS eigenfrequency responses δf_m (kHz) to toluene adsorption (blue) are depicted in detuning space (GHz). The optical spring induced eigenfrequency shifts $\delta f_{m,\ opt}$ (kHz) are displayed as a black curve together with a red shadow line representing the corrected frequency shift, $\delta f_{m,\ opt}$ - 456 Hz, both embedded in appropriate error bounds.

PLEASE CITE THIS ARTICLE AS DOI: 10.1063/1.5117159

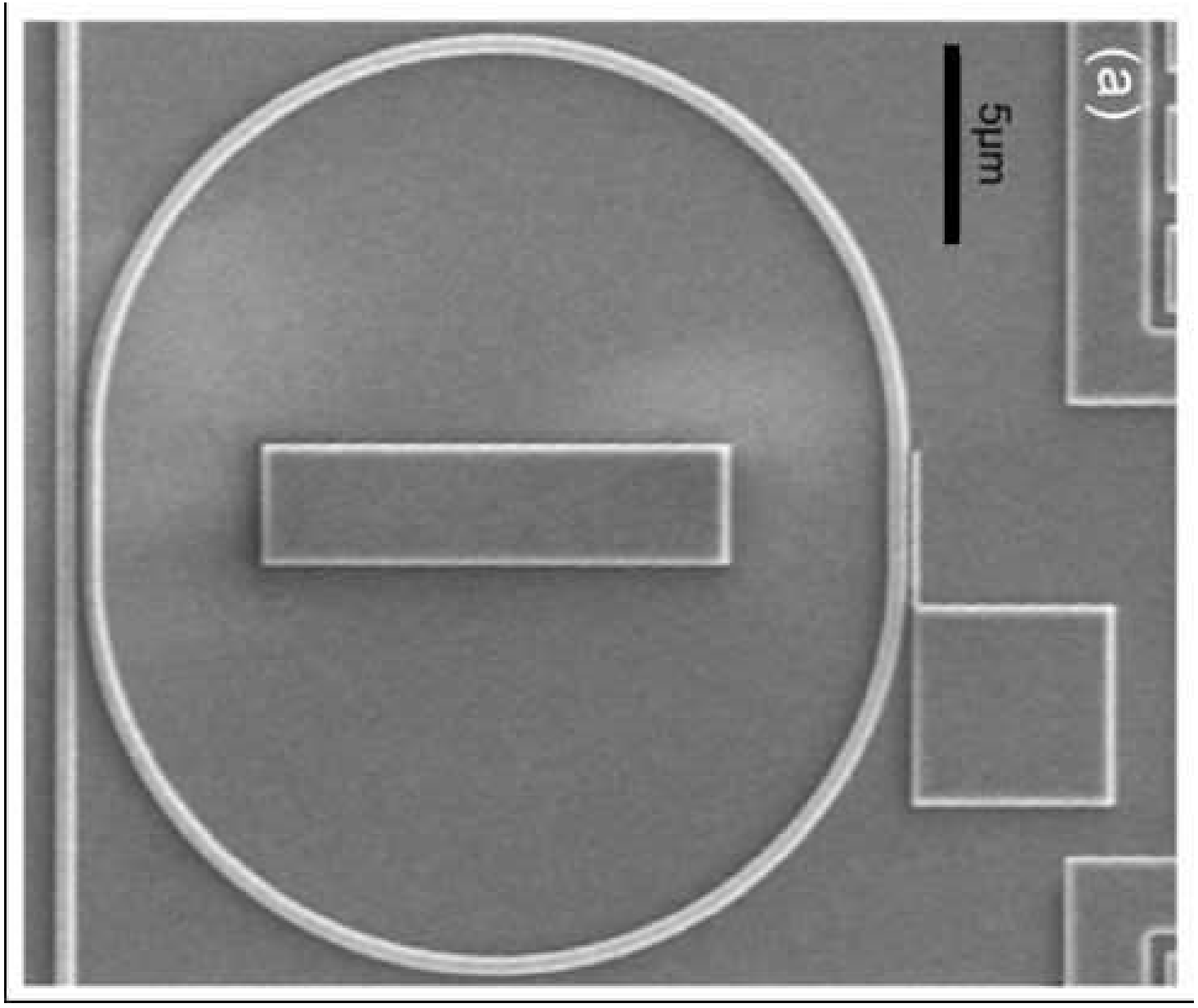

PLEASE CITE THIS ARTICLE AS DOI: 10.1063/1.5117159

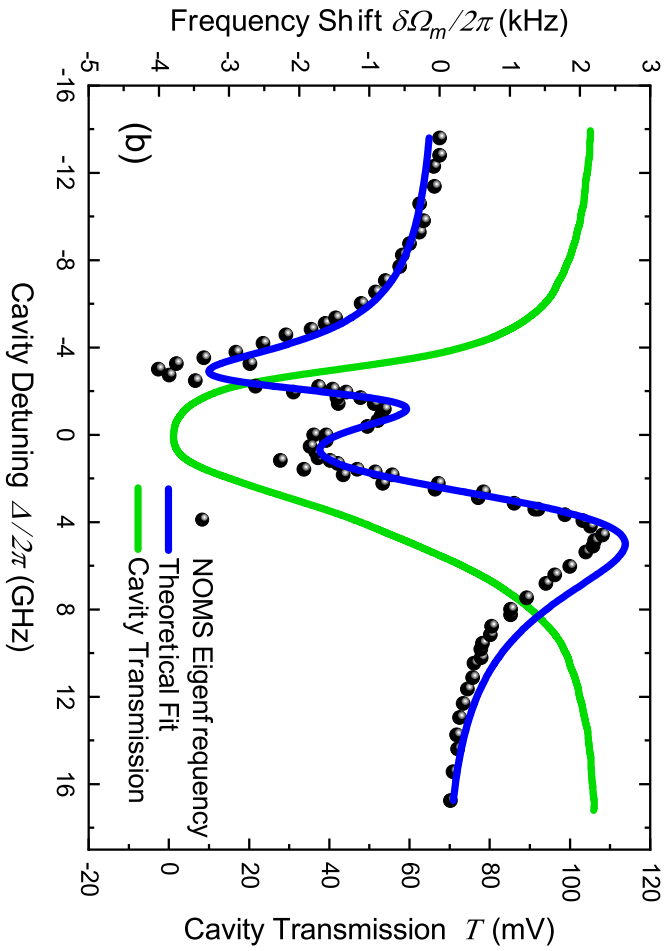

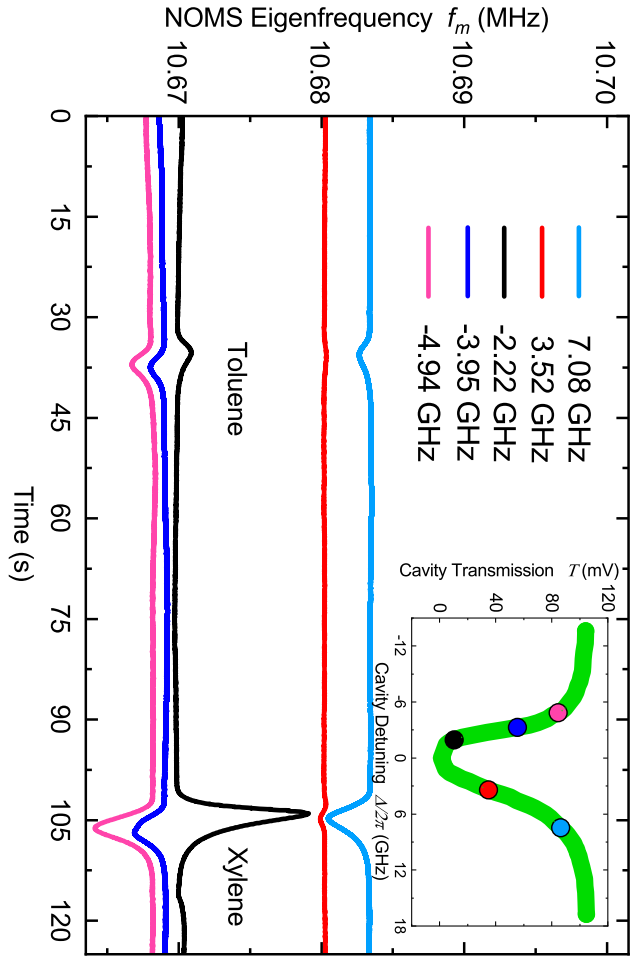

PLEASE CITE THIS ARTICLE AS DOI: 10.1063/1.5117159